Extended finite element method for cohesive crack growth

Nicolas Moës, Ted Belytschko

Extended finite element method for cohesive crack growth

Nicolas Moës *, Ted Belytschko *

Department of Mechanical Engineering, Northwestern University, 2145 Sheridan Road, Evanston, IL 60208, USA

The extended finite element method allows one to model displacement discontinuities which do not conform to interelement surfaces. This method is applied to modeling growth of arbitrary cohesive cracks. The growth of the cohesive zone is governed by requiring the stress intensity factors at the tip of the cohesive zone to vanish. This energetic approach avoids the evaluation of stresses at the mathematical tip of the crack. The effectiveness of the proposed approach is demonstrated by simulations of cohesive crack growth in concrete.

Keywords: Cohesive crack; Finite elements; Discontinuous approximation; Stress intensity factors; Size effect

1. Introduction

Linear elastic fracture mechanics (LEFM) is only applicable when the size of the fracture process zone (FPZ) at the crack tip is small compared to the size of the crack and the size of the specimen [1]. Other models must be used to take into account the FPZ. The cohesive crack model is the simplest of such models. In a cohesive crack, the propagation is governed by a traction–displacement relation across the crack faces near the tip. This model was introduced in the early sixties for metals by Dugdale [2] and Barenblatt [3]. In the late seventies, Hillerborg et al. [4] introduced the concept of fracture energy into the cohesive crack model and proposed a number of traction–displacement relationships for concrete.

The numerical simulation of cohesive crack growth may be carried out with several different approaches. Petersson [5] exploits a boundary integral formulation and uses an a priori discretization of the kernels relying on elastic finite element computations. More recently, a boundary element formulation was also used by Yand and Ravi-Chandar [6]. In the work of Belytschko et al. [7], a meshless approach (element-free galerkin) is used to model cohesive crack growth under dynamic loading.

In the modeling of cohesive fracture with the finite element method, two main strategies may be found in the literature: discrete interelement cracks and discrete intraelement cracks. In the first approach, the crack extends between elements and remeshing is necessary when the crack path is not known in advance. This approach has been used to model cohesive crack growth in concrete in Refs. [8–11] and to model crack

* Corresponding authors.
E-mail addresses: moes@tam.nwu.edu (N. Moës), tedbelytschko@northwestern.edu (T. Belytschko).

growth in ductile materials in Refs. [12,13]. In the work of Xu and Needleman [14] and Ortiz and Camacho [15], a cohesive zone is placed as an interelement in between each pair of neighboring elements in the mesh, see also Ref. [16]. Crack growth, crack branching or fragmentation is then a natural outcome of the initial boundary-value problem. The intraelement approach includes the incorporation of a discontinuous mode on an element level. It was used in Refs. [17–19] to model shear bands and in Refs. [20,21] to model cracks. A comparative study of such finite elements with embedded discontinuities may be found in Ref. [22]. The use of embedded discontinuities avoids remeshing as the crack (or shear band) propagates and belongs to the family of assumed strain methods. Stability issues need to be considered with these methods [22].

Recently, an extension of the finite element method called the extended finite element method (X-FEM) [23,24] has been developed to model arbitrary discontinuities in meshes (see also Ref. [25]). This extension exploits the partition of unity property of finite elements [26], which allows local enrichment functions to be easily incorporated into a finite element approximation while preserving the classical displacement variational setting.

The X-FEM models the discontinuity in a displacement field along the crack path, wherever this path may be located with respect to the mesh. This flexibility enables the method to simulate crack growth without remeshing. In the papers by Belytschko and Black [24] and Moës et al. [23], the crack surfaces were considered free of tractions. In the paper by Dolbow et al. [27] contact and friction was incorporated on the crack faces to simulate crack growth under compression. In the present paper, we extend the method to the case of crack growth involving a cohesive law on the crack faces and study its performance. The modeling of cohesive cracks using the partition of unity property of finite elements was also considered recently in Ref. [28].

2. Description of the problem

The description of the cohesive crack model will be decomposed into two parts. In the first part, the static, kinematic and constitutive equations characterizing the displacement and stress fields for a *given* location of the crack path are presented. In the second part, we express the conditions for crack growth and discuss the selection of the crack growth direction.

2.1. Variational formulation

Consider a domain Ω as shown in Fig. 1, containing a crack Γ_c. The part of the crack on which a cohesive law is active is denoted by Γ_{coh} and called the FPZ. Prescribed tractions, $\boldsymbol{F}$, are imposed on the boundary Γ_F whereas prescribed displacements (assumed to be zero for simplicity) are imposed on $\Gamma_{\boldsymbol{u}}$. The stress field inside the domain, $\boldsymbol{\sigma}$, is related to the external loading $\boldsymbol{F}$ and the closing tractions $\boldsymbol{t}^+$, $\boldsymbol{t}^-$ in the cohesive zone through the equilibrium equations:

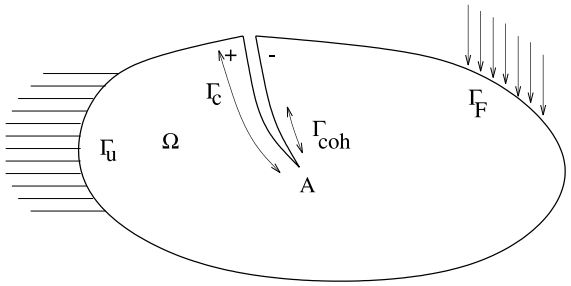

Fig. 1. Notations for a specimen with a crack involving a cohesive zone.

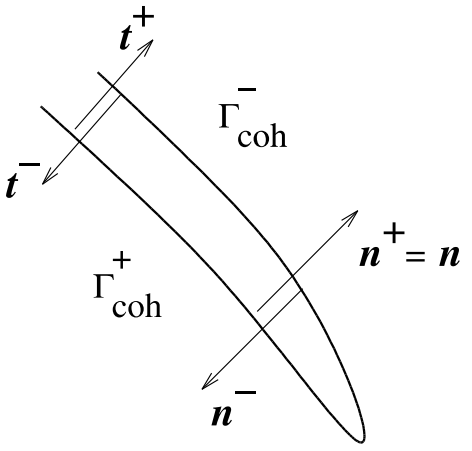

Fig. 2. Zoom in the region of the cohesive zone.

$$\nabla \cdot \boldsymbol{\sigma} = 0 \text{ on } \Omega, \quad \boldsymbol{\sigma} \cdot \boldsymbol{n} = \boldsymbol{F} \text{ on } \Gamma_F \tag{1}$$

$$\boldsymbol{\sigma} \cdot \boldsymbol{n}^+ = -\boldsymbol{\sigma} \cdot \boldsymbol{n}^- = \boldsymbol{t}^+ = -\boldsymbol{t}^- = \boldsymbol{t} \text{ on } \Gamma_{coh} \tag{2}$$

The orientation of the normals $\boldsymbol{n}^+$ and $\boldsymbol{n}^-$ are shown in Fig. 2.

The kinematic equations include the strain–displacement relationship, the prescribed displacement boundary conditions and the definition of the separation, $\boldsymbol{w}$, in the cohesive law. Under the assumptions of small strains and displacements, the kinematic equations read

$$\boldsymbol{\epsilon} = \tfrac{1}{2}(\nabla \boldsymbol{u} + (\nabla \boldsymbol{u})^T) \equiv \boldsymbol{\epsilon}(\boldsymbol{u}) \text{ on } \Omega, \quad \boldsymbol{u} = 0 \text{ on } \Gamma_u$$

$$\boldsymbol{w} = (\boldsymbol{u}^- - \boldsymbol{u}^+) \text{ on } \Gamma_{coh}$$

Finally, we need to give a constitutive law relating the cohesive tractions, $\boldsymbol{t} = \boldsymbol{t}^+ = -\boldsymbol{t}^-$, to the separation $\boldsymbol{w}$ in the cohesive zone and a constitutive law for the domain surrounding the crack. The latter law is assumed linear elastic and isotropic. The constitutive laws may thus be formally written

$$\boldsymbol{t} = \boldsymbol{t}(\boldsymbol{w}) \text{ on } \Gamma_{coh}, \quad \boldsymbol{\sigma} = \boldsymbol{C} : \boldsymbol{\epsilon} \text{ on } \Omega \tag{3}$$

where $\boldsymbol{C}$ is Hooke's tensor.

We now transform the strong form of the problem into a weak form better suited for finite element computations. The displacement $\boldsymbol{u}$ must belong to the set $\mathscr{U}$ of kinematically admissible displacement fields:

$$\boldsymbol{u} \in \mathscr{U} = \{\boldsymbol{v} \in \mathscr{V} : \boldsymbol{v} = \boldsymbol{0} \text{ on } \Gamma_u\} \tag{4}$$

The exact mathematical nature of the space $\mathscr{V}$ is related to the regularity of the solution. The $\mathscr{V}$ space allows for discontinuous displacements across the boundary Γ_c of the crack. The weak form of the equilibrium equations is

$$\int_\Omega \boldsymbol{\sigma} : \boldsymbol{\epsilon}(\boldsymbol{v}) \, d\boldsymbol{x} = \int_{\Gamma_F} \boldsymbol{F} \cdot \boldsymbol{v} \, d\boldsymbol{s} + \int_{\Gamma^+_{coh}} \boldsymbol{t}^+ \cdot \boldsymbol{v} \, d\boldsymbol{s} + \int_{\Gamma^-_{coh}} \boldsymbol{t}^- \cdot \boldsymbol{v} \, d\boldsymbol{s} \quad \forall \boldsymbol{v} \in \mathscr{U} \tag{5}$$

or, in a more compact form, owing to $\boldsymbol{t} = \boldsymbol{t}^+ = -\boldsymbol{t}^-$,

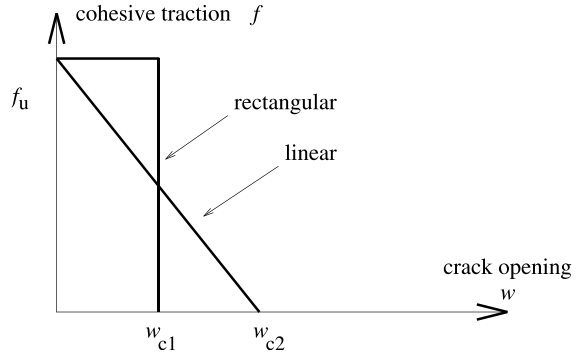

Fig. 3. Two cohesive laws with the same cohesive strength and fracture energy.

$$\int_{\Omega} \boldsymbol{\sigma} : \boldsymbol{\epsilon}(\boldsymbol{v}) \, \mathrm{d}\boldsymbol{x} + \int_{\Gamma_{\mathrm{coh}}} \mathbf{t} \cdot \boldsymbol{w}(\boldsymbol{v}) \, \mathrm{d}\boldsymbol{s} = \int_{\Gamma_{\mathrm{F}}} \boldsymbol{F} \cdot \boldsymbol{v} \, \mathrm{d}\boldsymbol{s} \quad \forall \boldsymbol{v} \in \mathscr{U} \tag{6}$$

where $\boldsymbol{w}(\boldsymbol{v}) = \boldsymbol{v}^- - \boldsymbol{v}^+$.

In the numerical studies, we shall consider cohesive crack growth in concrete. We neglect the shear component of the cohesive tractions as in Ref. [29] although this is not an intrinsic limitation of the method. In fact, we could have implemented a coupled (tension/shear) cohesive zone constitutive model (that of Tvergaard and Hutchinson [30] or that of Xu and Needleman [14]). Furthermore, we shall consider linear and rectangular cohesive laws, shown in Fig. 3 for which the cohesive law reads

$$f = f_{\mathrm{u}} - kw \tag{7}$$

where $f = \boldsymbol{t} \cdot \boldsymbol{n}$ and $w(\boldsymbol{v}) = \boldsymbol{w}(\boldsymbol{v}) \cdot \boldsymbol{n}$ is the normal separation. The slope of the cohesive law is the constant $-k$ ($k > 0$) for the linear profile and 0 ($k = 0$) for the rectangular case. Owing to two simplifications above, the variational principle (6) may be rewritten as

$$\int_{\Omega} \boldsymbol{C}\boldsymbol{\epsilon}(\boldsymbol{u}) : \boldsymbol{\epsilon}(\boldsymbol{v}) \, \mathrm{d}\boldsymbol{x} - \int_{\Gamma_{\mathrm{coh}}} kw(\boldsymbol{u})w(\boldsymbol{v}) \, \mathrm{d}\boldsymbol{s} = \int_{\Gamma_{\mathrm{F}}} \boldsymbol{F} \cdot \boldsymbol{v} \, \mathrm{d}\boldsymbol{s} - \int_{\Gamma_{\mathrm{coh}}} f_{\mathrm{u}} w(\boldsymbol{v}) \, \mathrm{d}\boldsymbol{s} \quad \forall \boldsymbol{v} \in \mathscr{U} \tag{8}$$

2.2. Cohesive crack growth

At any given time t_n the location of the FPZ is characterized by two tips: a mathematical tip where the crack opening is zero and a physical tip where the cohesive tractions are zero as shown in Fig. 4. Before any loading is applied to the specimen, these two tips coincide. As the loading is imposed, the FPZ develops. The cohesive traction at the mathematical tip is f_{u} whereas the crack opening at the physical tip is w_{c}.

In cohesive crack growth, snap-back may occur. The snap-back branch can be captured numerically only if the loading process is controlled by a monotonically increasing function of the crack length. Bocca et al. [9] suggest to use the crack length itself as the increasing function and call it a "crack length control scheme". This scheme is used here. Let us assume that the imposed tractions $\boldsymbol{F}$ depend linearly on a scalar parameter (load factor) λ: $\boldsymbol{F} = \lambda \boldsymbol{F}_0$. The problem to be solved is then stated as follows: given a cohesive zone extent Γ_{coh}, (Fig. 1) and the direction of extension (we shall discuss the crack growth direction subsequently) find the load factor λ such that $f = f_{\mathrm{u}}$ at the tip (meaning that A (Fig. 1) is indeed the mathematical tip). If the loading is too small, the cohesive zone will close before point A, if the loading is too high, the traction at the tip A will be lower than f_{u}. In finite element methods with cohesive zone discretely modeled by element edges, the value of f at the tip may be obtained from the nodal forces at the mathe-

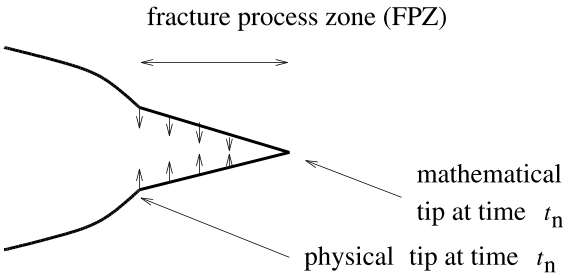

Fig. 4. The extent of the cohesive zone at time t_n.

matical tip or using elastic "dummy" (penalty) interface stiffness and calculating the stress at the integration points near the tip.

The previous paragraph describes one way to formulate the problem. The shortcoming of this formulation is that it involves quantities close to the tip A whose accuracy in the finite element context may be questionable. Instead of evaluating pointwise quantities, we prefer to rely on energetic considerations. The load factor is found such that the Mode I stress intensity factor (SIF) vanishes at the mathematical tip of the cohesive zone. Indeed, an important motivation behind the introduction of a cohesive zone in fracture mechanics is to avoid the non-physical, singular stress fields at the crack tip.

We restate the problem as follows: given a cohesive zone Γ_{coh} find the load factor λ such that the SIF K_{I} at the tip A is zero. The evaluation of K_{I} is carried out with a domain integral recalled in Appendix A. Note that the idea of using $K_{\text{I}} = 0$ as a crack tip stability criterion was also previously proposed in Ref. [10].

Let us now formalize the preceding idea and discuss the direction of propagation. Let θ be the direction of propagation of the mathematical tip in between the times t_n and t_{n+1} as shown in Fig. 5. The location of the mathematical tip at times t_n and t_{n+1} is denoted by $\boldsymbol{x}_n^{\text{tip}}$ and $\boldsymbol{x}_{n+1}^{\text{tip}}$, respectively. The load factor λ at time $t_n + 1$ is determined so that the mode I SIF is zero at the tip $\boldsymbol{x}_{n+1}^{\text{tip}}$. Since the bulk of the material is linearly elastic, this SIF is the sum of the SIF caused by the external loading $K_{\text{I}}^{\text{ext}}$ and the cohesive forces $K_{\text{I}}^{\text{coh}}$:

$$K_{\text{I}}(\lambda) = K_{\text{I}}^{\text{ext}}(\lambda) + K_{\text{I}}^{\text{coh}}(\lambda) = 0 \tag{9}$$

or

$$K_{\text{I}}^{\text{ext}}(\lambda) = -K_{\text{I}}^{\text{coh}}(\lambda) \tag{10}$$

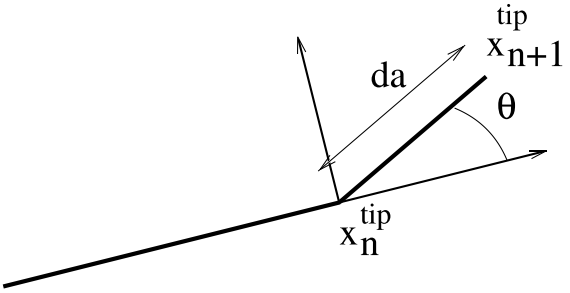

Fig. 5. Notations for a step of growth of the cohesive crack.

Note that in LEFM for a brittle material the right-hand side of Eq. (10) is replaced by the critical SIF K_{Ic}, which is a material property characterizing the toughness of the material:

$$K_{\mathrm{I}}^{\mathrm{ext}}(\lambda) = K_{\mathrm{Ic}} \tag{11}$$

Note also that the external SIF, $K_{\mathrm{I}}^{\mathrm{ext}}$, is linear in the loading factor λ whereas the cohesive SIF, $K_{\mathrm{I}}^{\mathrm{coh}}$, is non-linear in λ.

To determine the direction of crack propagation, we rely on LEFM. The use of LEFM criterion to predict trajectory of cohesive crack has been promoted in Refs. [31–33]. The LEFM theory introduces at least two criteria: the "principle of local symmetry" [34] and the "maximum hoop stress criterion" [35]. The principle of local symmetry requires that the angle θ be such that the second SIF is zero at the new tip $\boldsymbol{x}_{n+1}^{\mathrm{tip}}$. It is thus an implicit criterion. A way to implement it is to iterate on the crack growth direction until the second stress is close to zero. Note that these iterations would not require any remeshing since the mesh does not need to conform to the crack.

The maximum hoop stress criterion on the other hand is an explicit criterion which defines the direction of propagation to be along a direction normal to the maximum hoop stress. Using the work of Amestoy and Leblond [36], the maximum hoop stress and principle of local symmetry criteria may be compared for an infinitesimal crack growth. They are very close for small K_2/K_1 ratios and differ by at most 7° in the growth angle as K_2/K_1 becomes large.

Using the maximum hoop stress criteria, the angle of crack growth θ is expressed in terms of the external SIFs at the current tip $\boldsymbol{x}_n^{\mathrm{tip}}$ through the formula:

$$\theta = 2 \arctan \tfrac{1}{4}\left(K_{\mathrm{I}}^{\mathrm{ext}}/K_{\mathrm{II}}^{\mathrm{ext}} \pm \sqrt{(K_{\mathrm{I}}^{\mathrm{ext}}/K_{\mathrm{II}}^{\mathrm{ext}})^2 + 8} \right) \tag{12}$$

where the sign in Eq. (12) is chosen so that the hoop stress $\sigma_{\theta\theta}$ is positive. Note the ratio of the SIFs appearing in Eq. (12) does not depend on the load factor. The use of Eq. (12) with residual (near, but arbitrarily non-zero) values of K_{I} and K_{II} as a basis for trajectory prediction in arbitrary cohesive crack growth can also be found in Ref. [31].

In the numerical studies, the cohesive crack growth direction at each step will be determined by Eq. (12) as in Refs. [9,32,33], i.e. the crack path is determined by linear fracture theory, whereas the global load–deflection curve for the structure as the crack grows will be determined by the cohesive model. This assumption is in accordance with experiments on concrete in which it was observed that the size effect in concrete affects the load–deflection curves whereas the crack path is much less sensitive to the structure size.

3. The extended finite element discretization

The discretization of the displacement set $\mathscr{U}$ is accomplished by the extended finite element method which allows the crack location to be arbitrary with respect to the mesh. We shall here summarize the main idea of this extension. For a complete presentation see Ref. [23]. Fig. 6 shows a discontinuity (cohesive crack) placed on a structured and on an unstructured mesh. The classical finite element approximation on these meshes reads

$$\boldsymbol{u}^h = \sum_{i \in I} \boldsymbol{u}_i \phi_i \tag{13}$$

where I is the set of all nodes in the mesh; $\boldsymbol{u}_i$ is the classical (vectorial) displacement degree of freedom at node i and ϕ_i is the shape function associated with node i. Each shape function ϕ_i has compact support ω_i given by the union of the elements connected to node i. In the numerical studies the shape functions ϕ_i are linear (three-node triangle shape functions).

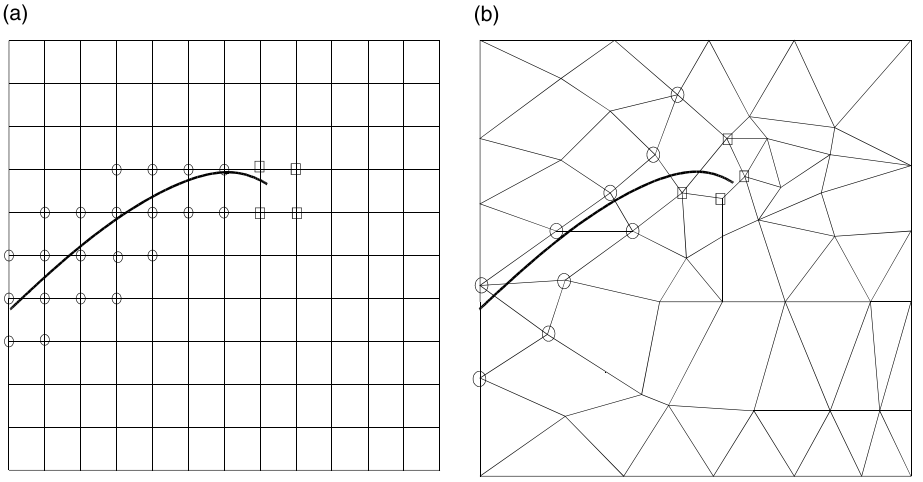

Fig. 6. Discontinuity on a structured mesh (a) and on an unstructured mesh (b). The circled nodes are enriched by the jump function H whereas the squared nodes are enriched by the branch tip functions F_l.

In order to model the presence of the discontinuity, the finite element approximation (13) is enriched by two additional terms

$$\boldsymbol{u}^h = \sum_{i\in I} \boldsymbol{u}_i \phi_i + \sum_{j\in J} \boldsymbol{b}_j \phi_j H(f(\boldsymbol{x})) + \sum_{k\in K} \phi_k \quad \sum_{l=1} \boldsymbol{c}_k^l F_l(\boldsymbol{x}) \Bigg) \tag{14}$$

The first additional term involves the jump function $H(\cdot)$:

$$H(x) = \begin{cases} -1 & \text{if } x > 0 \\ +1 & \text{if } x < 0 \end{cases} \tag{15}$$

and $f(\boldsymbol{x})$ is the signed distance function to the crack (the sign determining whether $\boldsymbol{x}$ is on one side or the other of the crack). The nodes "enriched" by the function H are such that their support (we mean the support of the nodal shape function) is bisected (cut into two separate pieces) by the crack. These nodes form the "J" set and are depicted with circles in Fig. 6.

The second additional term in Eq. (14) involve a set of branch functions $F_l(\boldsymbol{x})$ to model the displacement field around the tip of the discontinuity. In LEFM these functions are chosen based on the asymptotic features of the displacement field at the crack tip:

$$\{F_l(r,\theta)\} \equiv \left\{ \sqrt{r}\sin\left(\frac{\theta}{2}\right), \sqrt{r}\cos\left(\frac{\theta}{2}\right), \sqrt{r}\sin\left(\frac{\theta}{2}\right)\sin(\theta), \sqrt{r}\cos\left(\frac{\theta}{2}\right)\sin(\theta) \right\} \tag{16}$$

where (r,θ) are the local polar coordinates at the tip. To model a cohesive crack tip, we need alternative functions since the stresses at the tip are not singular. An asymptotic analysis of the mechanical fields in a cohesive zone for very large structure has been carried out in Refs. [37,38]. We shall consider the following branch functions:

$$\{F_l(r,\theta)\} \equiv r\sin\left(\frac{\theta}{2}\right) \quad \text{or} \quad r^{3/2}\sin\left(\frac{\theta}{2}\right) \quad \text{or} \quad r^2\sin\left(\frac{\theta}{2}\right) \tag{17}$$

Note that the use of non-singular branch functions within the X-FEM framework was already introduced in Ref. [39] and also suggested in Ref. [25]. The nodes enriched by the branch function form the set K and are shown as squares in Fig. 6. The support of these nodes contain the cohesive tip.

Finally, introducing the X-FEM approximation (14) in the displacement variational principle (8), we obtain the discrete variational principle: find $\boldsymbol{u}^h \in \mathscr{U}^h$ such that

$$\int_{\Omega} \boldsymbol{C}\boldsymbol{\epsilon}(\boldsymbol{u}^h) : \boldsymbol{\epsilon}(\boldsymbol{v})\,\mathrm{d}\boldsymbol{x} - \int_{\Gamma_{\mathrm{coh}}} kw(\boldsymbol{u}^h)w(\boldsymbol{v})\,\mathrm{d}\boldsymbol{s} = \lambda \int_{\Gamma_{\mathrm{F}}} \boldsymbol{F}_0 \cdot \boldsymbol{v}\,\mathrm{d}\boldsymbol{s} - \int_{\Gamma_{\mathrm{coh}}} f_{\mathrm{u}} w(\boldsymbol{v})\,\mathrm{d}\boldsymbol{s} \quad \forall \boldsymbol{v} \in \mathscr{U}^h \tag{18}$$

In Eq. (18), the load factor λ appears explicitly. The dimension of the discrete displacement space, $\mathscr{U}^h$, depends on the number of nodes in the mesh and the number of additional degrees of freedom to model the presence of the crack ($\boldsymbol{b}_j$ and $\boldsymbol{c}_k^l$ in Eq. (14)).

The left hand side of the discrete displacement variational principle (18) involves an integration over the domain and an integration over the cohesive zone. The integration over the domain is performed element by element. For the element cut by the discontinuity, the integration is performed on each side of the discontinuity separately [23]. For the integration over the cohesive zone, the zone is geometrically represented by a sequence of 1D segments. The integration is thus performed by looping over these segments [27]. Four Gauss points are used on each segment for an accurate integration of the branch functions. Fig. 7 shows a mesh and a sequence of 1D segments representing the cohesive zone on the mesh.

The flowchart for the cohesive crack growth simulation is as follows:

- Step 0: Initially, a mesh and the location of the crack (or possibly no crack at all) are given.
- Step 1: The direction of propagation is obtained using Eq. (12) and a segment of length da (user defined) is added to the cohesive zone. An initial guess for the load factor (user defined) is also provided. In the case where no crack is initially present, the first segment starts at a point and with an orientation determined by the location and plane on which the tensile strength f_{u} is reached first.
- Step 2: Given a load factor solve for the displacement field using Eq. (18). Note that this equation is linear.
- Step 3: If on the last 1D segment (away from the tip) the crack opening at all integration points is bigger than the critical opening remove this 1D segment from the cohesive zone and repeat Step 2. The critical opening is w_{c1} or w_{c2} depending on the cohesive law considered; see Fig. 3.
- Step 4: Compute the K_{I} SIF at the tip.
- Step 5: If K_{I} is zero within some user defined tolerance go to Step 1. If not, update the load factor λ (a secant method is used) and go to Step 2.

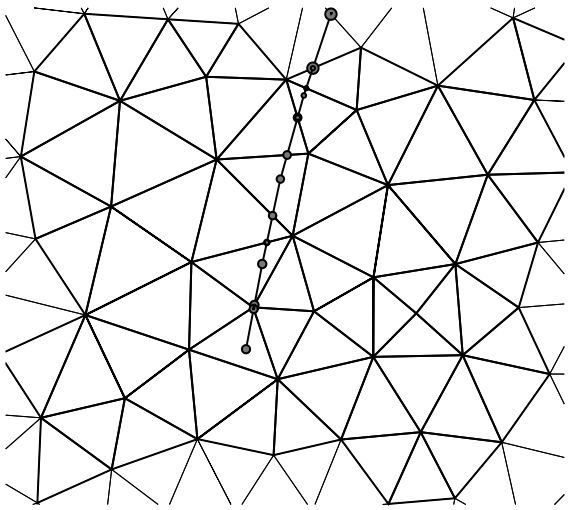

Fig. 7. A zoom on the mathematical tip of a cohesive zone showing the 1D segments delimited with dots.

Concerning the implementation of the X-FEM, at least two aspects need to be taken care of. The first one deals with the existence of enriched nodes and the second one is the integration on elements cut by the crack or close to the crack tip. Concerning the existence of enriched nodes, our finite element object (C++ implementation) may have an arbitrary number of degrees of freedom (dof) and each dof is aware of the nature of its shape function. The expression of the stiffness matrix at the element level is detailed in Ref. [40]. On the elements cut by the crack, we integrate separately the stiffness matrix on each side of the crack using a strategy introduced in Ref. [23]. On the elements close to the crack tip, a higher order quadrature rule is used [23].

4. Numerical studies

In the numerical experiments, we consider two different concrete specimens: a three-point bending beam in which the cohesive crack propagates in a straight line and a four-point shear bending in which the crack path is curved.

4.1. A three-point bending specimen

Consider the beam in three-point bending shown in Fig. 8. The growth of a cohesive crack in such a specimen has been studied extensively by Carpinteri and Colombo [41] using finite element analysis and the node release technique. This load–deflection curve is shown in Fig. 10 for the following geometrical parameters

$$b = 0.15 \text{ m}, \quad l = 4b, \quad t = b, \quad a = 0 \tag{19}$$

(t is the specimen thickness) and the following material properties

$$E = 36,500 \text{ MPa}, \quad v = 0.1, \quad f_u = 3.19 \text{ MPa} \tag{20}$$

where E is the Young's modulus, v the Poisson's ratio and f_u the cohesive strength. The fracture energy is $G_F = 50 \text{ N m}^{-1}$ and the cohesive profile is linear (see Fig. 3). To eliminate rigid body motion in the x direction, the point $(0, b/2)$ is allowed to move only in the y direction. Note that $a = 0$ in the geometric description of the problem, (Eq. (19)), indicates that there is initially no crack in the beam. As the load increases the cohesive zone starts developing at the bottom midpoint of the beam when the cohesive strength, f_u, is reached.

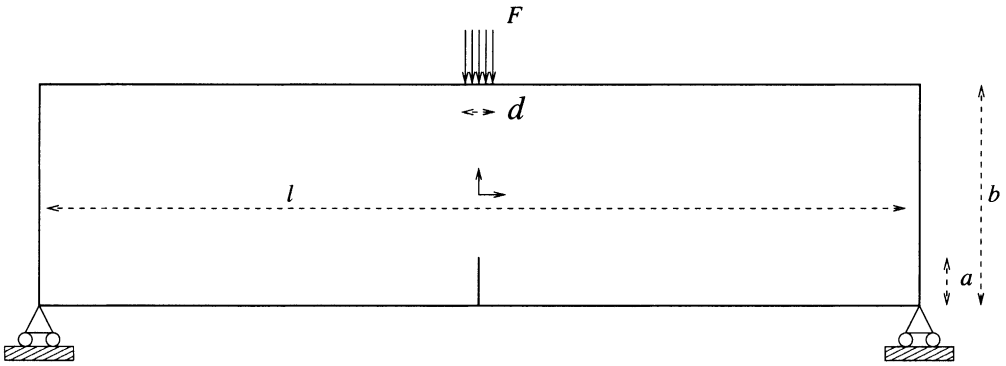

Fig. 8. A three-point bending specimen.

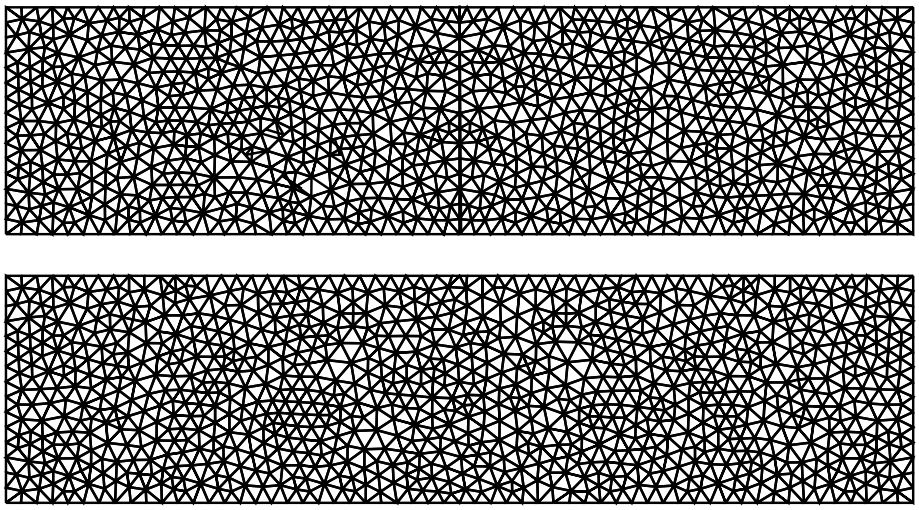

Fig. 9. A mesh matching (above) and non-matching (below) the crack path.

The load–deflection points obtained with X-FEM are shown in Fig. 10. Two different meshes, shown in Fig. 9, are considered: a mesh matching the cohesive zone and a mesh not matching the cohesive zone. Fig. 10 also compares the influence of the choice of the branch functions (17). We observe that the X-FEM results are consistent whether or not the mesh matches the cohesive crack path and are quite close for three different choices of the branch function. In the remainder of this paper, only the branch function $r\sin\theta/2$ will be considered. The X-FEM results are also very close to the results in Ref. [41]. Note that our numerical simulation was carried out under the plane strain assumption whereas the results in Ref. [41] were obtained under a plane stress assumption. We believe these two assumptions are close for a Poisson's ratio

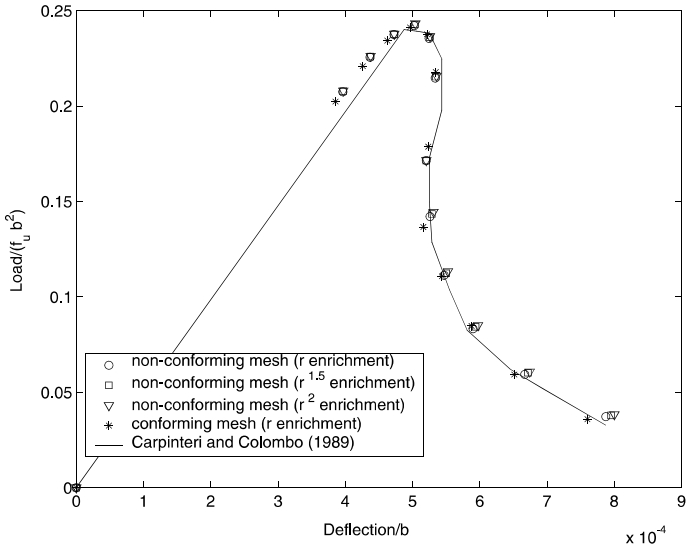

Fig. 10. Non-dimensional load–deflection curves for the three-point bending specimen ($G_F = 50\ \mathrm{N\,m^{-1}}$).

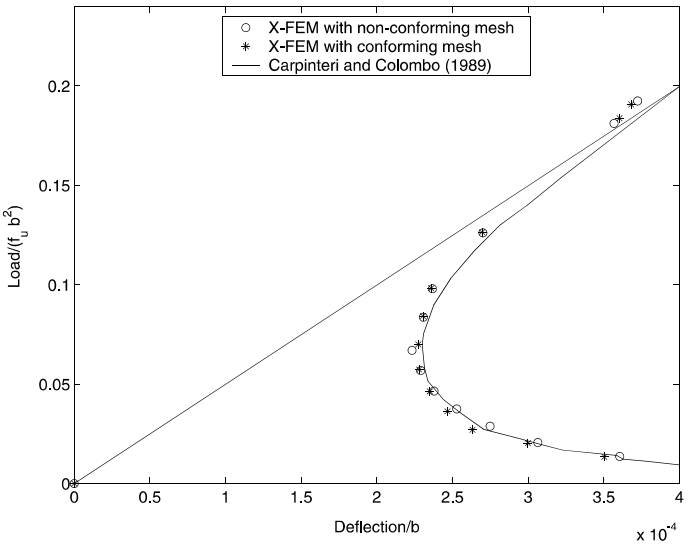

Fig. 11. Non-dimensional load–deflection curves for the three-point bending specimen ($G_F = 5\ \mathrm{N\,m^{-1}}$).

of 0.1. Also, we have distributed the load over a length of $d = 0.01$ m, (see Fig. 8), whereas a concentrated load was considered in Ref. [41].

Fig. 11 shows another comparison between X-FEM and the numerical simulation of Carpinteri and Colombo [41] for a sharper snap-back (the fracture energy is now $G_F = 5\ \mathrm{N\,m^{-1}}$).

We now use X-FEM to analyze the size effect phenomenon. Fig. 12 shows the non-dimensional load–deflection curve for different brittleness number, s_E

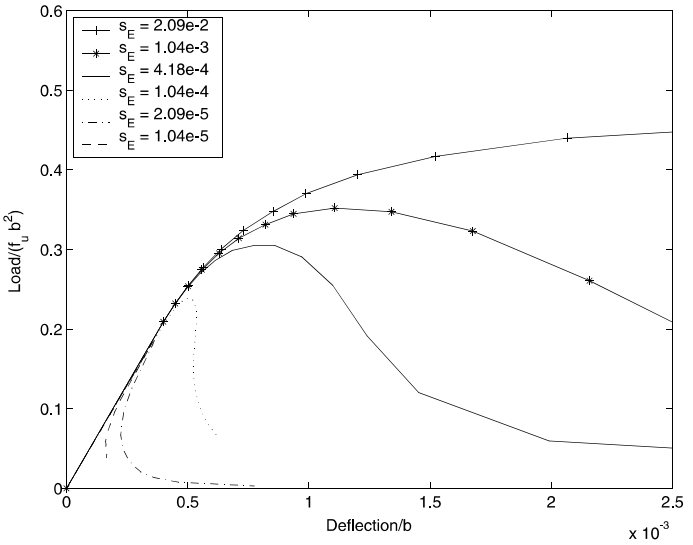

Fig. 12. Non-dimensional load–deflection curves to analyze the size effect in the three-point bending specimen.

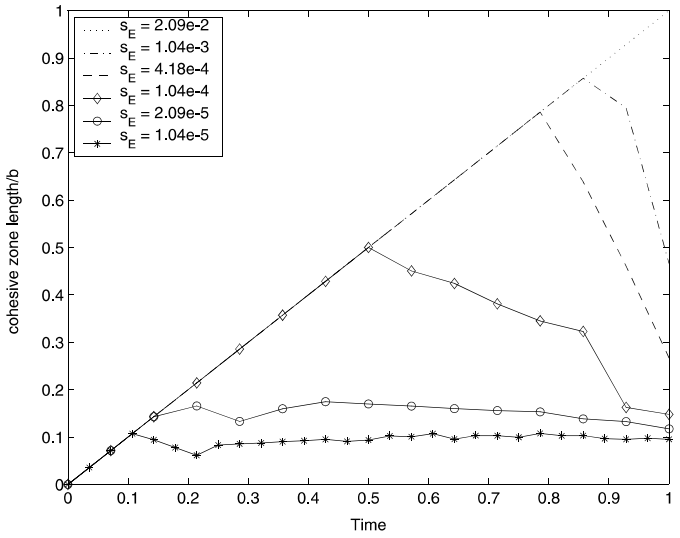

Fig. 13. Evolution of the size of the cohesive zone length as the mathematical tip travels through the beam (normalized by the depth of the beam b).

$$s_E = \frac{G_F}{f_u b} \tag{21}$$

This non-dimensional number has been introduced by Carpinteri [42] to compare the brittleness of different specimens with the same ratio f_u/E. The higher s_E, the more ductile the specimen is as observed in Fig. 12 (s_E should thus better be called a ductility number as noted by Bažant and Planas [1]: the smaller the specimen, the more ductile it is). A higher s_E means a smaller structure size b or a higher fracture energy G_F.

Fig. 13 shows the evolution of the size of the cohesive zone (relative to the beam depth) as the mathematical tip travels through the beam. The time 1.0 on the abscissa corresponds to the time at which the tip has reached the top surface of the beam. We observe that the ductile specimens tend to develop a very long cohesive zone (in the extreme case, $s_E = 2.09e^{-2}$, the full extent of the beam depth) whereas the cohesive zone is quite small for brittle specimens. At the limit of $s_E \to 0$, the cohesive zone reduces to a "point" (the crack tip) and linear fracture mechanics is recovered.

Carpinteri and Colombo [41] carried out a numerical study to determine the influence of the mesh refinement on the quality of the results for different brittleness number s_E. They used meshes of four-node quadrilaterals and three-node triangles. For the three-point bending problem, they found that the element size h must satisfy Eq. (22) to obtain reasonable load–deflection curves:

$$h \leqslant 600 w_c \tag{22}$$

where w_c if the critical opening for the linear cohesive law. We may rewrite the condition (22) as a condition on the number of element, N_c, needed per characteristic length l_{ch} of the material:

$$N_c \equiv l_{ch}/h \geqslant 10 \tag{23}$$

The material characteristic length is defined by

$$l_{ch} = \frac{G_F E}{(1-\nu^2) f_u^2}$$

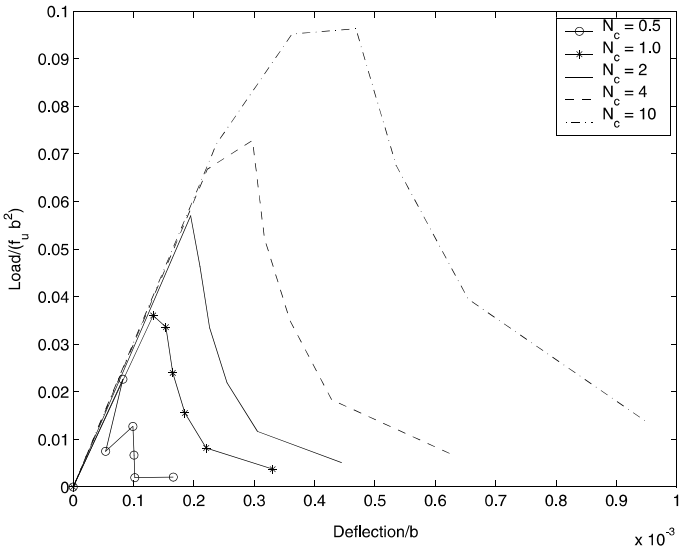

Fig. 14. Non-dimensional load–deflection curves for a uniform mesh (10 elements in the depth and 40 in the length). The number of element per characteristic length N_c is varied by modifying the fracture energy.

and is of the order of the size of the cohesive zone. Thus, in the finite element approach with node release, at least 10 elements are needed to cover the characteristic length of the material.

We carried out a similar numerical investigation with X-FEM. An easy way to change the ratio N_c is to work with a given mesh and vary G_F. The non-dimensional load–deflection curves obtained with X-FEM are shown in Fig. 14 for a uniform mesh (10 elements in the depth, 40 in the length of the beam) and Fig. 15 for the unstructured mesh shown in Fig. 9 (below).

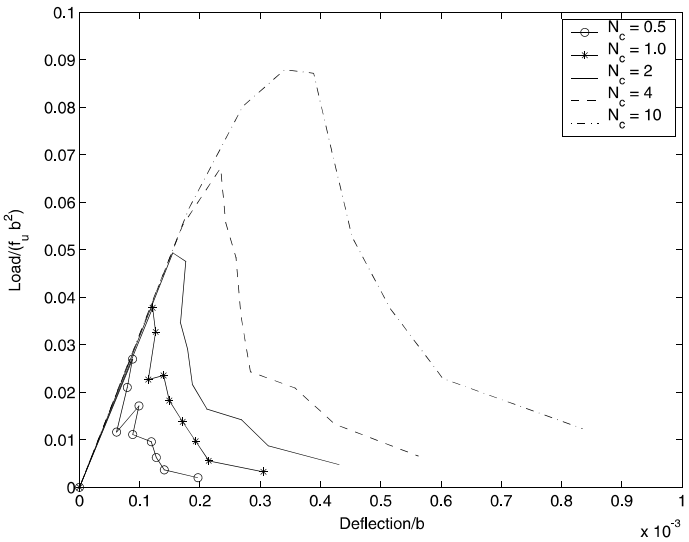

Fig. 15. Non-dimensional load–deflection curves for an unstructured mesh shown in Fig. 9 (below). The number of element per characteristic length $N_c = l_{ch}/h$ is varied by modifying the fracture energy.

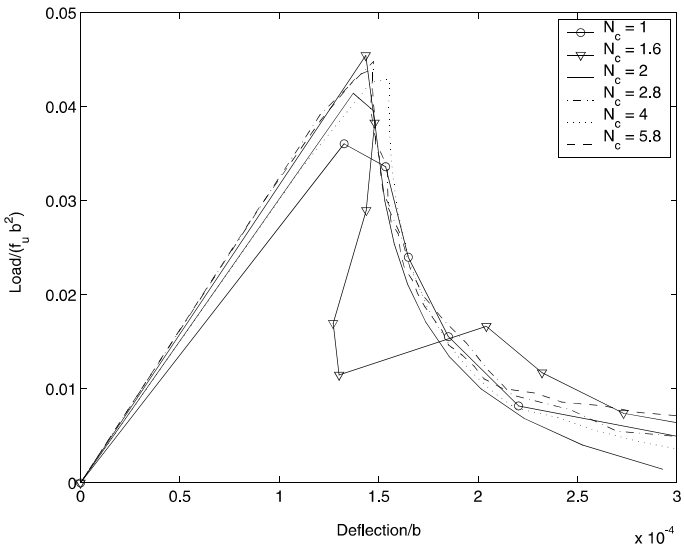

Fig. 16. Non-dimensional load–deflection curves obtained with different meshes for a fixed fracture energy ($G_F = 4.14\ \mathrm{N\,m^{-1}}$).

In each simulation, the crack is grown by an amount da at each step where da is the characteristic element size in the mesh. The initial crack length $a = 0.3b$ and the material properties are still given by Eq. (20). We observe that above a threshold of about two elements per characteristic length, the results are stable. Note that the results for N_c below 0.5 are not shown because they are subjected to large oscillations. Similar oscillations were observed by Carpinteri and Colombo [41] even for N_c in the range of 1–10, where our method succeeded.

Fig. 16 shows the load–deflection curves obtained with different meshes (uniform and unstructured) and a fixed fracture energy ($G_F = 4.14\ \mathrm{N\,m^{-1}}$). As in Figs. 14 and 15, a minimum of about two elements per characteristic length is needed to obtain reliable results.

4.2. A four-point shear specimen

This numerical example is taken from Ref. [29] and shown in Fig. 17. The geometrical characteristics of the problem are

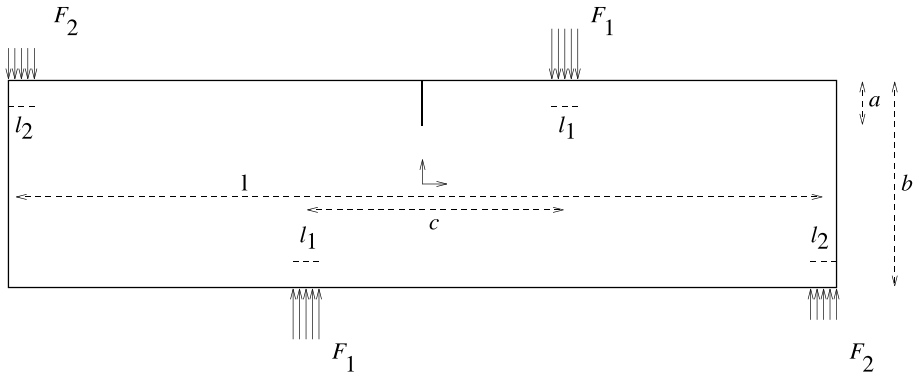

Fig. 17. A four-point shear specimen.

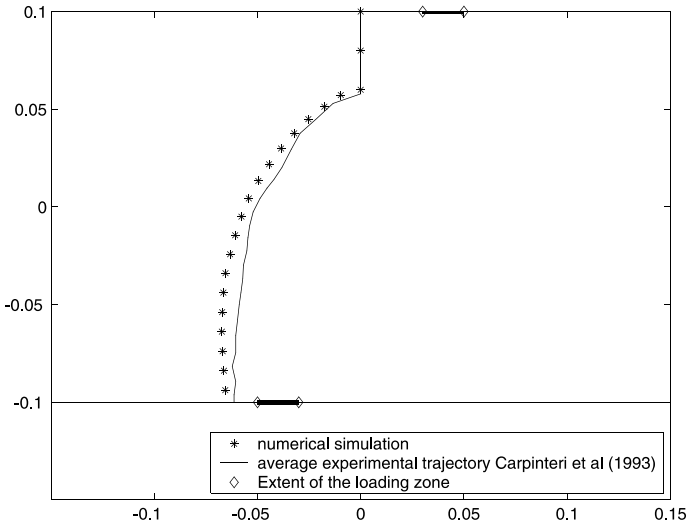

Fig. 18. Comparison between experimental results and the X-FEM numerical simulation for the crack path.

$$b = 0.2 \text{ m}, \quad l = 4b, \quad a = 0.2b, \quad c/b = 0.4, \quad l_1 = l_2 = 0.02 \text{ m}, \quad t = 0.10 \text{ m}$$

where t is the specimen thickness and the material parameters are

$$E = 28,000 \text{ MPa}, \quad v = 0.1, \quad G_F = 145 \text{ N m}^{-1}, \quad f_u = 2.4 \text{ MPa}$$

The point $(l/2, -b/2)$ is fixed in both x and y directions whereas the point $(-c/2, -b/2)$ is fixed in the y direction. The mesh consists of about 11,000 nodes and we consider 18 steps of crack growth each of size 0.01 m. A comparison in between experimental (average) crack path and the path obtained with X-FEM is shown in Fig. 18.

As the crack is propagating, the number of nodes enriched with the jump function rises from 24 to 130 (dof associated with the $\boldsymbol{b}_j$, Eq. (14)). On the other hand, the number of nodes enriched with the tip function (dof of type $\boldsymbol{c}_k$), remains roughly constant (around 3).

As the cohesive crack propagates, the load–deflection curve where F_1 and F_2 are applied are shown in Fig. 19. The experimental curves are taken from Ref. [29]. A very severe snap-back is observed under the load F_1.

In Fig. 20, we compare the load–deflection curves obtained with X-FEM for linear fracture mechanics and two different cohesive law profiles: rectangular and linear. In all three cases, the fracture energy is the same: $G_F = 145 \text{ N m}^{-1}$. The load in Fig. 20 is the total load on the upper part of the beam $F_1 + F_2$ whereas the deflection is the average

$$\frac{(l - l_2)\delta_1 + c\delta_2}{(l - l_2) + c} \tag{24}$$

where δ_1 and δ_2 is the (average) deflection in the loading zones 1 and 2, respectively. Figs. 21 and 22 show the cohesive crack at four different steps of the propagation.

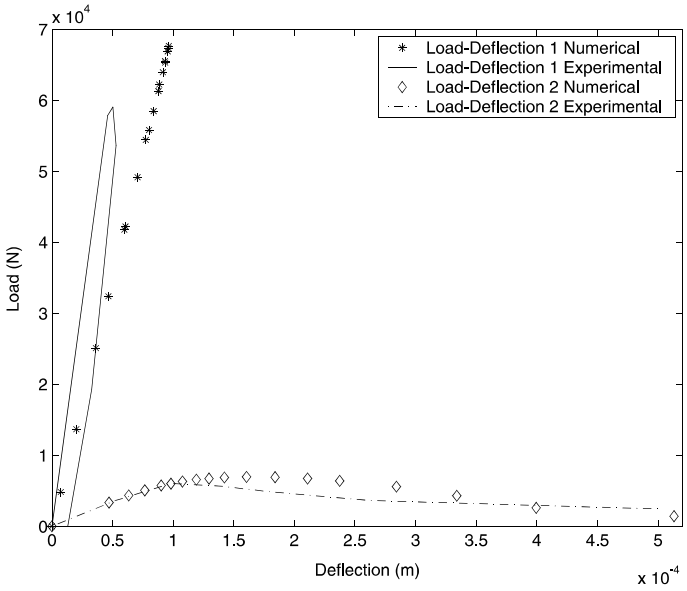

Fig. 19. Load–deflection curves in the first and second loading zones for the four-point shear problem.

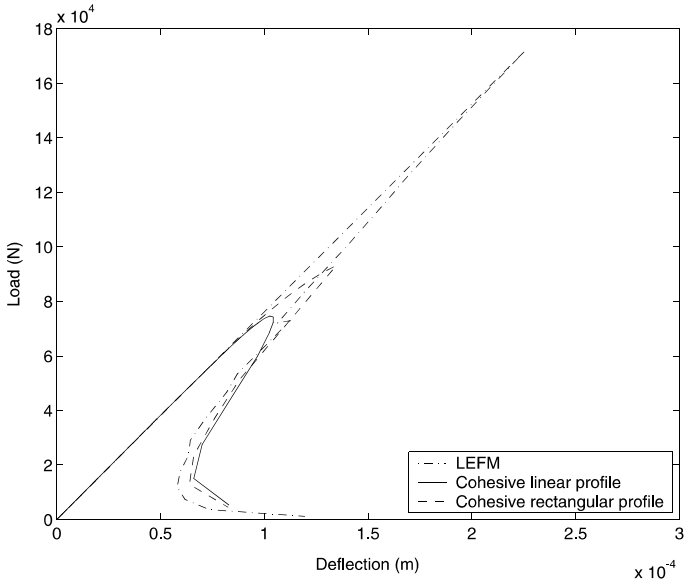

Fig. 20. Load–deflection curve for the four-point shear specimen considering linear fracture mechanics and two different cohesive law profiles.

5. Conclusions

A method has been developed to allow smooth growth of cohesive cracks in finite elements meshes without remeshing. The problem of finding the proper load factor for a given crack growth does not involve

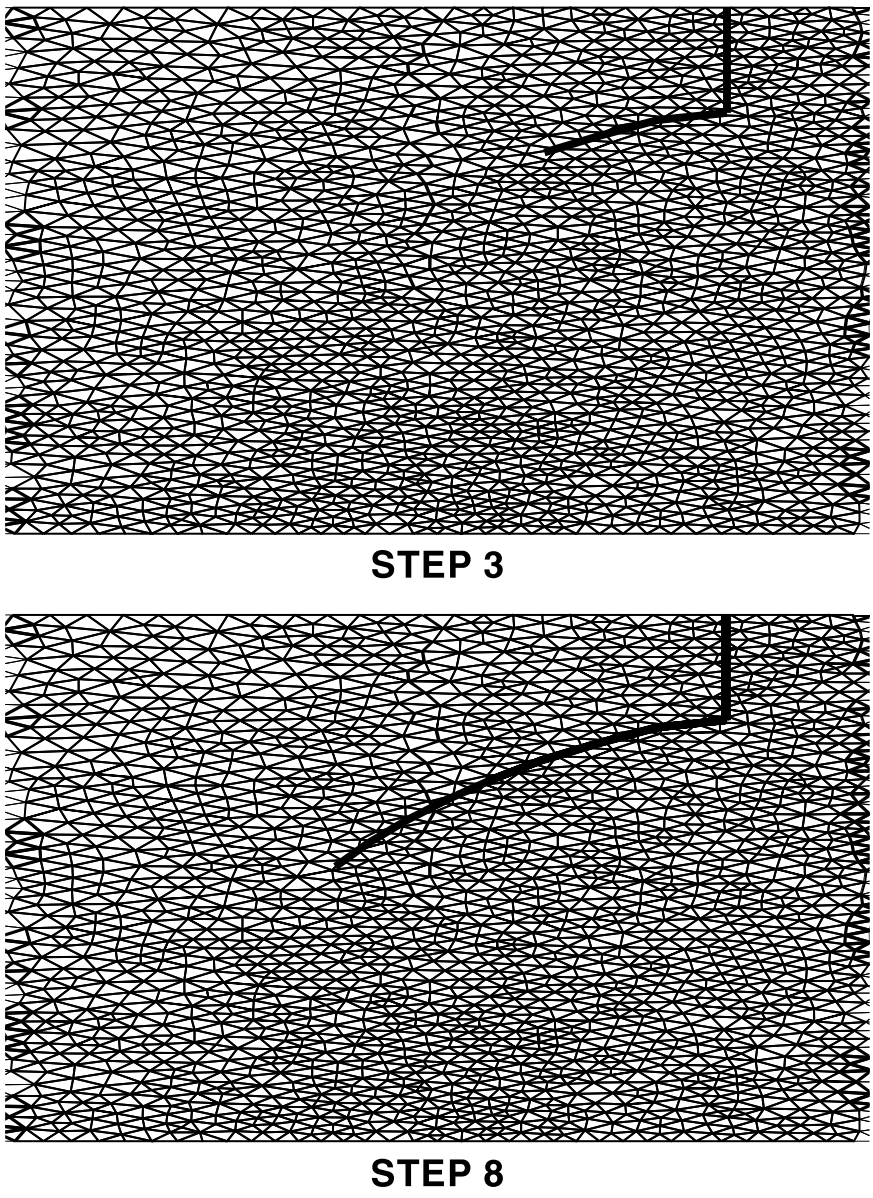

Fig. 21. Extent of the cohesive crack at steps 3 and 8 of the propagation. The axis have been stretched for a better rendering.

the evaluation of the stress field at the mathematical tip of the cohesive zone. Instead we rely on energetic considerations: the correct load factor is found by zeroing the Mode I SIF at the tip. The numerical studies carried out for the three-point bending specimen indicate that the proposed approach (X-FEM in conjunction with *J*-domain integral) is more accurate than the classical finite element approach with node release (and stress evaluation at the tip) in the sense that fewer elements are needed per characteristic length of the material (around two elements instead of 10 in the node release case). Also, no remeshing is required as the crack propagates since with the X-FEM approach, the location of the crack may be arbitrary with respect to the mesh.

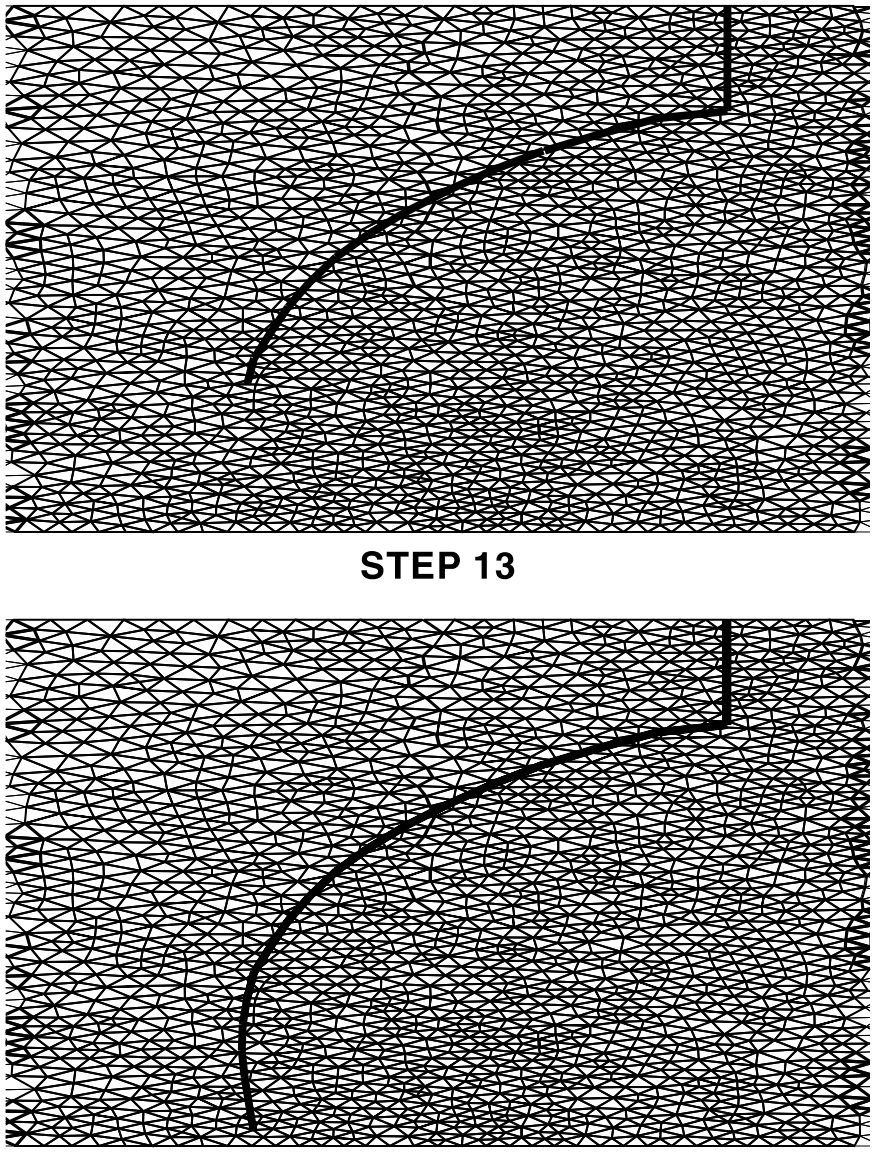

Fig. 22. Extent of the cohesive crack at steps 13 and 18 of the propagation. The axis have been stretched for a better rendering.

Acknowledgements

The support of the Office of Naval Research and Army Research Office, to Northwestern University, is gratefully acknowledged. We are also grateful to J. Dolbow, B. Moran and G. Ventura for their comments and suggestions.

Appendix A. Two-dimensional interaction integral for a curved loaded crack

In linear elasticity, the general form of the J-contour integral for a crack not necessarily straight and in the presence of tractions on the crack faces is given by

$$J = \int_{\Gamma \cup \Gamma_{c+} \cup \Gamma_{c-}} \left(\frac{1}{2} \sigma_{ik} \epsilon_{ik} \delta_{1j} - \sigma_{ij} u_{i,1} \right) n_j \, \mathrm{d}s \tag{A.1}$$

The coordinate system is taken to be the local crack tip coordinate system with the x_1 axis tangent to the crack at the tip, see Fig. 23. The scalar n_j is the j component of the outward normal to the closed contour $\Gamma \cup \Gamma_{c+} \cup \Gamma_{c-}$ and $\delta_{1j} = 1$ if $j = 1$ and 0 otherwise. The J integral is contour independent and measures the strength of the singularity at the crack tip:

$$J = \frac{K_{\mathrm{I}}^2}{E^*} + \frac{K_{\mathrm{II}}^2}{E^*} \tag{A.2}$$

where $E^* = E$ (Young's modulus) for plane stress and $E^* = E/(1 - \nu^2)$ for plane strain (ν is the Poisson's ratio).

This contour integral may be turned into a domain integral, more suited for finite element computations [43,44]. Defining a scalar function q which takes a value of unity on an open set containing the crack tip and vanishes on an outer prescribed contour (Γ here), the contour integral (25) may be recast into the domain integral:

$$J = \int_A \left(\sigma_{ij} u_{i,1} - \frac{1}{2} \sigma_{ik} \epsilon_{ik} \delta_{1j} \right) q, j \, \mathrm{d}\boldsymbol{x} + \int_{\Gamma_{c+} \cup \Gamma_{c-}} \left(\frac{1}{2} \sigma_{ik} \epsilon_{ik} \delta_{1j} - \sigma_{ij} u_{i,1} \right) q n_j \, \mathrm{d}s \tag{A.3}$$

It is possible to use the J-integral concept to extract separately the stress intensity factors K_{I} and K_{II} [45]. Two states of a cracked body are considered. State 1 $(\sigma_{ij}^{(1)}, \epsilon_{ij}^{(1)}, u_i^{(1)})$ corresponds to the present state and State 2 $(\sigma_{ij}^{(2)}, \epsilon_{ij}^{(2)}, u_i^{(2)})$ is an auxiliary state which will be chosen as the asymptotic fields for Mode I or Mode II. The J-integral for the sum of the two states is

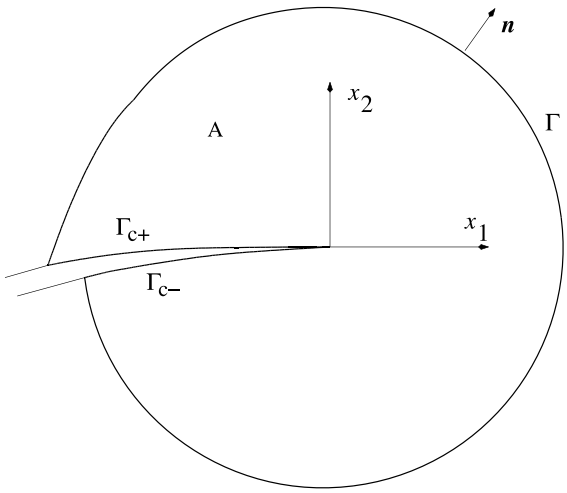

Fig. 23. Notations for the J-integral.

$$J^{(1+2)} = J^{(1)} + J^{(2)} + I^{(1,2)}$$
$$= \frac{(K_{\mathrm{I}}^{(1)})^2}{E^*} + \frac{(K_{\mathrm{II}}^{(1)})^2}{E^*} + \frac{(K_{\mathrm{I}}^{(2)})^2}{E^*} + \frac{(K_{\mathrm{II}}^{(2)})^2}{E^*} + \frac{2}{E^*}\left(K_{\mathrm{I}}^{(1)}K_{\mathrm{I}}^{(2)} + K_{\mathrm{II}}^{(1)}K_{\mathrm{II}}^{(2)}\right) \tag{A.4}$$

from which we deduce

$$I^{(1,2)} = \frac{2}{E^*}(K_{\mathrm{I}}^{(1)}K_{\mathrm{I}}^{(2)} + K_{\mathrm{II}}^{(1)}K_{\mathrm{II}}^{(2)}) \tag{A.5}$$

where $I^{(1,2)}$, called the interaction integral for States 1 and 2, is given by

$$I^{(1,2)} = \int_A (\sigma_{ij}^{(1)}u_{i,1}^{(2)} + \sigma_{ij}^{(2)}u_{i,1}^{(1)} - \sigma_{ik}^{(1)}\epsilon_{ik}^{(2)}\delta_{1j})q,j \,\mathrm{d}\boldsymbol{x} + \int_{\Gamma_{c+}\cup\Gamma_{c-}} (\sigma_{ik}^{(1)}\epsilon_{ik}^{(2)}\delta_{1j} - \sigma_{ij}^{(1)}u_{i,1}^{(2)} - \sigma_{ij}^{(2)}u_{i,1}^{(1)})qn_j \,\mathrm{d}s \tag{A.6}$$

Making the judicious choice of State 2 as the pure Mode I asymptotic fields with $K_{\mathrm{I}}^{(2)} = 1$, $K_{\mathrm{II}}^{(2)} = 0$ gives the Mode I SIF for State 1 in terms of the interaction integral

$$K_{\mathrm{I}}^{(1)} = \frac{2}{E^*}I^{(1,\mathrm{Mode\ I})} \tag{A.7}$$

The mathematical proof of the contour independence of the integrals presented above assumes that the fields σ, ϵ and u (and the auxiliary fields) satisfy exactly the equation of the problem. In practice, the finite element solution does not satisfy these equations. The domain integral is nevertheless a robust tool to extract the stress intensity factors. Similarly, the auxiliary field taken as the Mode I or Mode II asymptotic fields are only approximate solution in the case of a curved crack. Accurate results are nevertheless obtained.

For the numerical evaluation of the above integral, the domain A is set from the collection of elements about the crack tip. We first determine the characteristic length of an element touched by the crack tip and designate this quantity as h_{local} [23]. For two dimensional analysis, this quantity is calculated as the square root of the element area. The domain A is then set to be all elements which have a node within a ball of radius r_{d} about the crack tip where r_{d} is taken as $2h_{\mathrm{local}}$ in the numerical experiments.

References

[1] Bažant ZP, Planas J. Fracture and size effect in concrete and other quasibrittle materials. Boca Raton: CRC Press; 1998.
[2] Dugdale DS. Yielding of steel sheets containing slits. J Mech Phys Solids 1960;8:100–8.
[3] Barenblatt GI. The mathematical theory of equilibrium of cracks in brittle fracture. Adv Appl Mech 1962;7:55–129.
[4] Hillerborg A, Modéer M, Petersson PE. Analysis of crack formation and crack growth in concrete by means of fracture mechanics and finite elements. Cement and Concrete Research 1976;6(6):163–8.
[5] Petersson P-E. Crack growth and development of fracture zone in plain concrete and similar materials Technical report TVBM-1006. Sweden: Lund Institute of Technology; 1981.
[6] Yang B, Ravi-Chandar K. A single-domain dual-boundary-element formulation incorporating a cohesive zone model for elastostatic cracks. Int J Fract 1998;93:115–44.
[7] Belytschko T, Organ D, Gerlach C. Element-free galerkin methods for dynamic fracture in concrete. Comp Meth Appl Mech Engng 2000;187:385–99.
[8] Carpinteri A. Post-peak and post-bifurcation analysis of cohesive crack propagation. Engng Fract Mech 1989;32:265–78.
[9] Bocca P, Carpinteri A, Valente S. Mixed mode fracture of concrete. Int J Solids Struct 1991;27:1139–53.
[10] Bittencourt TN, Ingraffea AR, Llorca J. Simulation of arbitrary cohesive crack propagation. In: Bažant ZP, editor. Fracture mechanics of concrete structures. Amsterdam: Elsevier; 1992. p. 339–50.
[11] Reich R, Červenka J, Saouma V. Merlin: a computational environment for 2d/3d discrete fracture analysis. In: Mang H, Bicanic N, de Borst R, editors. Computational modeling of concrete structures. Swansea: Pineridge press; 1994. p. 999–1008.
[12] Tvergaard V, Hutchinson J. Effect of strain-dependent cohesive zone model on predictions of crack growth resistance. Int J Solids Struct 1996;33:3297–308.

[13] Gullerud AS, Gao X, Dodds RH, Haj-Ali R. Simulation of ductile crack growth using computational cells: numerical aspects. Engng Fract Mech 2000;66:65–92.
[14] Xu X-P, Needleman A. Numerical simulations of fast crack growth in brittle solids. J Mech Phys Solids 1994;42(9):1397–434.
[15] Camacho GT, Ortiz M. Computational modelling of impact damage in brittle materials. Int J Solids Struct 1996;33:2899–938.
[16] Tijssens MGA, Sluys BLJ, van der Giessen E. Numerical simulation of quasi-brittle fracture and damaging cohesive surfaces. Eur J Mech A/solids 2000;19:761–79.
[17] Ortiz M, Leroy Y, Needleman A. Finite element method for localized failure analysis. Comp Meth Appl Mech Engng 1987;61(2):189–214.
[18] Belytschko T, Fish J, Englemann BE. A finite element method with embedded localization zones. Comp Meth Appl Mech Engng 1988;70:59–89.
[19] Simo JC, Oliver J, Armero F. An analysis of strong discontinuities induced by strain-softening in rate-independent inelastic solids. Comput Mech 1993;12:277–96.
[20] Lofti HR, Shing PB. Embedded representation of fracture in concrete with mixed finite element. Int J Numer Meth Engng 1995;38:1307–25.
[21] Oliver J. Modelling strong discontinuities in solid mechanics via strain softening constitutive equations. part 2: Numerical simulation. Int J Numer Meth Engng 1996;39:3601–23.
[22] Jirásek M. Comparative study on finite elements with embedded discontinuities. Comp Meth Appl Mech Engng 2000;188(1):307–30.
[23] Moës N, Dolbow J, Belytschko T. A finite element method for crack growth without remeshing. Int J Numer Meth Engng 1999;46:131–50.
[24] Belytschko T, Black T. Elastic crack growth in finite elements with minimal remeshing. Int J Numer Meth Engng 1999;45(5):601–20.
[25] Belytschko T, Moës N, Usui S, Parimi C. Arbitrary discontinuities in finite elements. Int J Numer Meth Engng 2001;50:993–1013.
[26] Melenk JM, Babuška I. The partition of unity finite element method: basic theory and applications. Comp Meth Appl Mech Engng 1996;39:289–314.
[27] Dolbow J, Moës N, Belytschko T. An extended finite element method for modeling crack growth with frictional contact. Comp Meth Appl Mech Engng, accepted for publication.
[28] Wells GN, Sluys LJ. A new method for modelling cohesive cracks using finite elements. Int J Numer Meth Engng 2001;50:2667–82.
[29] Carpinteri A, Valente S, Ferrara G, Melchiorri G. Is mode II fracture energy a real material property. Comput Struct 1993;48:397–413.
[30] Tvergaard V, Hutchinson JW. Relation between crack growth resistance and fracture process parameters in elastic–plastic solids. J Mech Phys Solids 1992;40(6):1377.
[31] Ingraffea AR, Gerstle W, Gergely P, Saouma V. Fracture mechanics in bond reinforced concrete. J Struct Div (ASCE) 1984;110(4):871–90.
[32] Garcia VO, Gettu R, Carol I. Numerical analysis of mixed mode fracture using interface elements. Proceedings of the European Congress on Computational Methods in Applied Sciences and Engineering (ECCOMAS 2000), Barcelona, Spain, 2000.
[33] Cendón DA, Gálvez JC, Elices M, Planas J. Modeling the fracture of concrete under mixed loading. Int J Fract 2000;103:293–310.
[34] Goldstein RV, Salganik RL. Brittle fracture of solids with arbitrary cracks. Int J Fract 1974;10:507–23.
[35] Erdogan G, Sih GC. On the crack extension in plates under plane loading and transverse shear. J Basic Engng ASME 1963;85:519–27.
[36] Amestoy M, Leblond JB. Crack paths in plane situation-II. detailed form of the expansion of the stress intensity factors. Int J Solids Struct 1992;29(4):465–501.
[37] Planas J, Elices M. Asymptotic analysis of a cohesive crack. 1. Theoretical background. Int J Fract 1992;55:153–77.
[38] Planas J, Elices M. Asymptotic analysis of a cohesive crack. 2. Influence of the softening curve. Int J Fract 1993;64:221–37.
[39] Dolbow J, Moës N, Belytschko T. Discontinuous enrichment in finite elements with a partition of unity method. Finite Elements Anal Des 2000;36:235–60.
[40] Sukumar N, Moës N, Belytschko T, Moran B. Extended finite element method for three-dimensional crack modelling. Int J Numer Meth Engng 2000;48(11):1549–70.
[41] Carpinteri A, Colombo G. Numerical analysis of catastrophic softening behavior (snap-back instability). Comput Struct 1989;31:607–36.
[42] Carpinteri A. Notch sensitivity in fracture testing of aggregative materials. Engng Fract Mech 1982;16:467–81.
[43] Destuynder P, Djaoua M, Lescure S. Some remarks on elastic fracture mechanics (quelques remarques sur la mécanique de la rupture élastique. Journal de Mécanique théorique et appliquée 1983;2(1):113–35.
[44] Moran B, Shih CF. Crack tip and associated domain integrals from momentum and energy balance. Engng Fract Mech 1987;127:615–42.
[45] Yau J, Wang S, Corten H. A mixed-mode crack analysis of isotropic solids using conservation laws of elasticity. J Appl Mech 1980;47:335–41.